- 40. C.-Y. Kao, E.-C. Cao, H. L. Wai, S.-C. Cheng, Nucleic Acids Res. 49, 9965-9977 (2021).
- 41. C. Cretu et al., Nat. Commun. 12, 4491-15 (2021).
- 42. Z. Zhang et al., Nature 596, 296-300 (2021).

### **ACKNOWLEDGMENTS**

We thank M. Pfleiderer and D. Peter for experimental advice: A. Fraudeau and E. Marchal for technical assistance: S. Schneider. E. Pellegrini, and W. Hagen for ensuring smooth running of the EMBL cryo-EM facilities; EMBL Proteomic Core Facility for performing mass spectrometry experiments; M. Pelosse and A. Aubert (EMBL EEF facility) for assistance with cell culture; M. Pezet (IAB Grenoble Flow Cytometry Platform) for cell sorting; A. Peuch and the FMBL Grenoble IT team for the support with high-performance computing; C. Query for an insightful discussion; and R. Pillai and S. Fica for critical comments on the manuscript. Funding: This project has received funding from the European Research Council (ERC) under the European Union's Horizon 2020 research and innovation programme (grant agreement no. 950278, awarded to W.P.G.). M.R. was supported by a fellowship from the EMBL Interdisciplinary Postdoc (EIPOD) programme under Marie Sklodowska-Curie Actions COFUND (grant agreement no. 847543). Author contributions: Conceptualization: J.T., W.P.G.; Methodology: J.T., M.R., F.W., W.P.G.; Investigation: J.T., M.R.; Visualization: J.T., W.P.G.; Funding acquisition: W.P.G.; Project administration: J.T., W.P.G.; Supervision: W.P.G.; Writing original draft: J.T., W.P.G.; Writing - review & editing: J.T., M.R., F.W., W.P.G. Competing interests: The authors declare that they have no competing interests. Data and materials availability: Cryo-EM maps were deposited in the EMDB with the following accession codes: EMD-13793 (17S U2 snRNP core); EMD-13810 (17S U2 snRNP HEAT repeats); EMD-13811 (A-like U2 snRNP); EMD-13813 (A-like U2 snRNP medium resolution/SF3B6 map); EMD-13812 (remodeled U2 snRNP); EMD-13815 (merged datasets the highest resolution map); EMD-13814 (AMP-PCP A-like U2 snRNP). Atomic coordinates were deposited in the PDB database

with the following accession codes: 7Q3L (17S U2 snRNP); 7Q4O (A-like U2 snRNP); 7Q4P (remodeled U2 snRNP). Materials generated in this study are available on request from the lead contact (wgalej@embl.fr).

### SUPPLEMENTARY MATERIALS

science.org/doi/10.1126/science.abm4245 Materials and Methods Figs. S1 to S9 Tables S1 and S2 References (43-69) MDAR Reproducibility Checklist Movies S1 and S2

17 September 2021: accepted 11 November 2021 Published online 25 November 2021 10.1126/science.abm4245

# REPORTS

# **GEOPHYSICS**

# On the relative temperatures of Earth's volcanic hotspots and mid-ocean ridges

Xiyuan Bao<sup>1</sup>\*, Carolina R. Lithgow-Bertelloni<sup>1</sup>, Matthew G. Jackson<sup>2</sup>, Barbara Romanowicz<sup>3</sup>

Volcanic hotspots are thought to be fed by hot, active upwellings from the deep mantle, with excess temperatures ( $T_{\rm ex}$ ) ~100° to 300°C higher than those of mid-ocean ridges. However,  $T_{\rm ex}$  estimates are limited in geographical coverage and often inconsistent for individual hotspots. We infer the temperature of oceanic hotspots and ridges simultaneously by converting seismic velocity to temperature. We show that while ~45% of plume-fed hotspots are hot ( $T_{ex} \ge 155^{\circ}$ C), ~15% are cold ( $T_{ex} \le 36^{\circ}$ C) and ~40% are not hot enough to actively upwell (50°C ≤ T<sub>ex</sub> ≤ 136°C). Hot hotspots have an extremely high helium-3/helium-4 ratio and buoyancy flux, but cold hotspots do not. The latter may originate at upper mantle depths. Alternatively, the deep plumes that feed them may be entrained and cooled by small-scale convection.

n Earth's surface, two types of volcanism are observed. The dominant type, observed at tectonic plate boundaries, manifests the large-scale global circulation in Earth's mantle. In contrast, isolated intraplate volcanoes, such as those of Hawaii, Iceland, or the Galápagos, do not fit with classical plate tectonics theory and are thought to reflect dynamical processes rooted in the deep mantle. The lavas found at these "hotspot" volcanoes provide a singular window into the thermochemical dynamics of Earth's interior. These hotspots usually appear as chains of intraplate volcanoes that may reflect relative movement between plates and the underlying mantle (1). The presence of active, hot, upwelling plumes rising from the core-mantle boundary (CMB) to the bottom of the lithosphere under hotspot volcanoes has been intensely debated (2,3) since it was

proposed 50 years ago (1). Nonetheless, the idea of hot mantle plumes originating in the deep mantle that sample sources distinct from those that give rise to mid-ocean ridge volcanism reconciles many geophysical and geochemical observations. For example, seismic studies showing an expected thinner mantle transition zone under hotspots (4, 5)and low-velocity columns in tomographic models that extend from the surface to the CMB beneath most hotspots (6) suggest that plumes can indeed extend well into the deep mantle. Geochemically distinct signals can be observed between ocean island basalts (OIBs) at hotspots and mid-ocean ridge basalts (MORBs), reflecting their source regions. MORBs have relatively uniform  ${}^{3}\text{He}/{}^{4}\text{He}$  ratios,  $\sim 8 \pm 1$  Ra (atmospheric ratio) (7) (10), whereas OIBs have a much wider range, with ratios up to 43 Ra in Iceland (8) [and up to 50 Ra at the Baffin Island large igneous province (9)]. The high  ${}^{3}\text{He}/{}^{4}\text{He}$ at hotspots might reflect a deep reservoir that preserves ancient Hadean material (10). Hotspots with high <sup>3</sup>He/<sup>4</sup>He are also those with the highest buoyancy flux, a measure of plume strength (11). High <sup>3</sup>He/<sup>4</sup>He signals and high buoyancy flux suggest a deep origin and active upwellings, which are further confirmed by the correlation between low shear wave velocities  $(V_S)$  at 200 km and high  ${}^3\text{He}/{}^4\text{He}$  signals at hotspots (12). If the low seismic velocities are dominantly thermal, it implies that hotspots with higher <sup>3</sup>He/<sup>4</sup>He anomalies are hotter and sufficiently buoyant to entrain the possibly denser high <sup>3</sup>He/<sup>4</sup>He domain (12, 13) from the deep mantle.

Classical plume theory predicts focused thermal anomalies beneath hotspots. Directly measuring the excess temperature of the subhotspot mantle relative to the mantle upwelling beneath ridges may therefore allow us to constrain the origin and dynamics of plumes that feed them. Previous temperature estimates using petrological thermometers suggest that the subhotspot mantle is typically 100° to 300°C hotter than the subridge mantle (4, 14, 15). This implies an excess temperature  $(T_{ex})$  for hotspots compared with ridges, where  $T_{\rm ex}$  is the difference between the potential temperature  $(T_p)$ —the temperature a parcel of mantle will have at Earth's surface if extrapolated along an adiabat-beneath an individual hotspot and the average ridge temperature  $\overline{T_{\rm p}}$ over all ridge segments. Dynamically, a  $T_{\rm ex}$  of between 100° and 150°C beneath the lithosphere is needed for pure thermal plumes of ~100 km radius to rise fast enough (~10 cm/year) in the upper mantle (16) to avoid cooling too much by diffusion, still create excess melt, and have enough buoyancy to continue rising (17). This estimate provides a dynamical limit for the minimum  $T_{\rm ex}$  and is coincidentally the same as the lower bound of typical petrological estimates (i.e.,  $T_{\rm ex} = 100\,{\rm ^{o}C}$ ). The question of whether all oceanic hotspots exceed the average ridge temperature and the minimum dynamic limit is hard to answer from petrological thermometers alone, given the limited geographical coverage and inconsistent estimates. Only a subset of hotspots (≤28) have petrological temperature estimates, and values vary substantially between studies (4, 14, 15). Estimates of the average temperature at mid-ocean ridges range from 1280° to 1400°C (4, 14, 15, 18, 19).

Department of Earth, Planetary, and Space Sciences, University of California, Los Angeles, CA 90095, USA. <sup>2</sup>Department of Earth Science, University of California, Santa Barbara, CA 93106, USA. <sup>3</sup>Department of Earth and Planetary Science, University of California, Berkeley, CA 94720 USA

<sup>\*</sup>Corresponding author. Email: xiyuanbao@g.ucla.edu

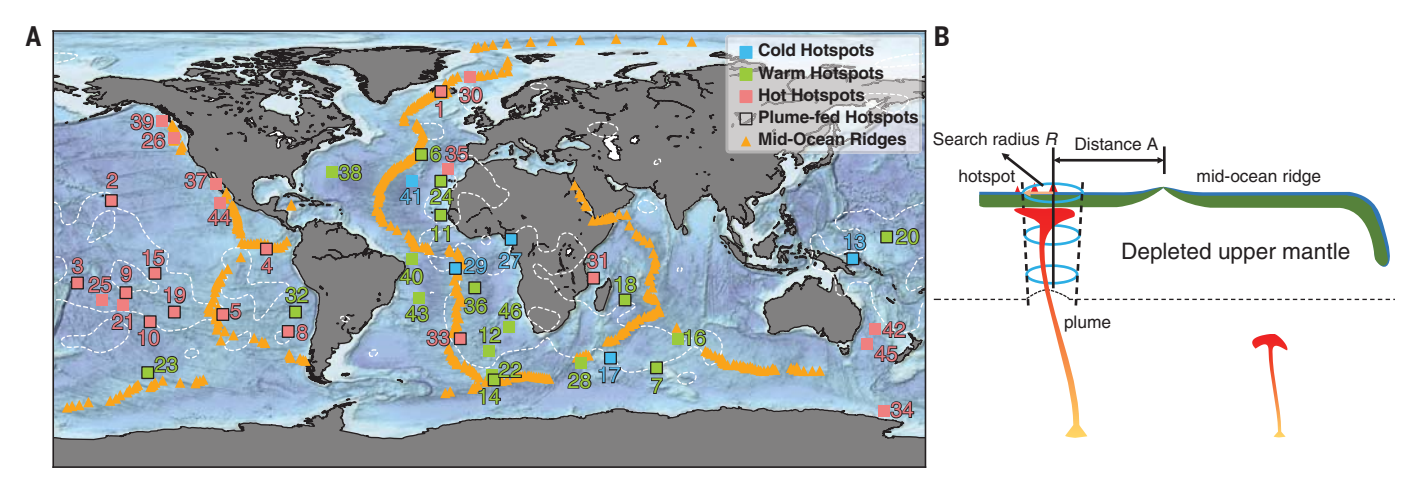
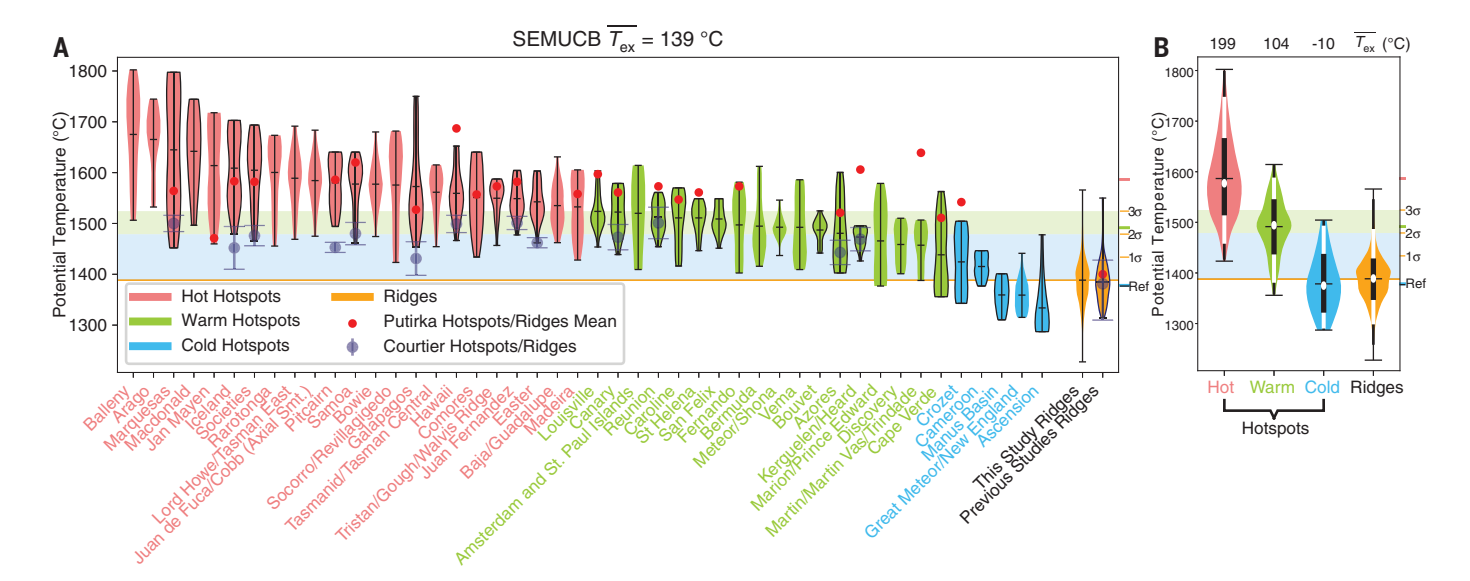


Fig. 1. Map of global hotspots and mid-ocean ridges and schematic of velocity extraction. (A) Red, green, and blue squares represent hot, warm, and cold oceanic hotspots, respectively. Squares with black outlines have resolved plumes (6). The numbers correspond to the hotspot IDs in data S1. Orange triangles show mid-ocean ridges. The -1%  $\delta lnV_S$  contour

at the CMB (22) represents LLSVPs in white dashed lines. (**B**) Sketch illustrating our search strategy. Radius R decreases with depth to account for the mantle's decreasing volume. Distance A defines the ridge-hotspot proximity threshold, used in (21). We use A = 1000 km and R = 500 km (21).



**Fig. 2. Potential temperature of oceanic hotspots and ridges.** Violin plots of the distribution of potential temperature  $(T_p)$ . (**A**) On the right side, the 1377°C reference adiabat (21) is marked by a black tick. Three yellow ticks indicate  $\overline{T_p} + 1\sigma$ ,  $2\sigma$ , and  $3\sigma$  for ridges. The width of the violin represents the probability density of temperature estimates from all depths (260 to 600 km). In every violin, horizontal bars, from top to bottom, are maximum, mean, and minimum values. Black outlines are plume-fed hotspots. From left to right, hotspots are arranged in order of decreasing  $T_p$ . Red, green, and blue violins are hot, warm, and cold hotspots, respectively, classified by cluster analysis, with ticks on

the right showing their  $\overline{T_{\rm ex}}$ . The blue shaded region ( $T_{\rm ex} < 2\sigma$ ) covers plumes that cannot actively upwell, green ( $2\sigma < T_{\rm ex} < 3\sigma$ ) covers those that barely can. Olivine thermometry estimates from Courtier *et al.* (4) for hotspots and ridges in purple [average and  $1\sigma$ , see (21)] and Putirka's (14) in solid red circles. Ridge estimates from this study and Dalton *et al.* (19) (with purple outlines) shown by yellow violins on the right. (B) Violin stacks for three clusters of hotspots compared with ridges (yellow).  $\overline{T_{\rm ex}}$  for each group shown on top. White circles are the median values, black and white bars away from the center indicate the central 68th, 95th, and 99.7th percentiles.

In this study, we reexamined whether oceanic hotspots are hotter than ridges using complete ridge segment (N=424) (20) and oceanic hotspot (N=46) (5, 12) catalogs (data S1 and Fig. 1A). We inferred temperature directly from seismic tomography in the upper mantle by converting velocity to temperature, similarly to Dalton *et al.* (19) for ridges. Dalton *et al.* (19) converted velocity to temperature at 300 km

depth below ridges, but not hotspots, and Jackson  $et\ al.\ (12)$  did not convert to temperatures and focused only on hotspots at 200 km depth. Examining both hotspots and ridges simultaneously is key to both computing excess temperatures and comparison with previous studies using petrological thermometers (14). We choose to compute  $T_{\rm ex}$  with respect to the ridge  $\overline{T_{\rm p}}$  in keeping with previous work

(14, 15) and understanding of MORB formation (21). For both ridges and hotspots, we inferred  $T_{\rm p}$  in 20-km intervals from 260 to 600 km depth, below the depths with the highest seismic attenuation (21). Hereafter we refer to potential temperature as temperature. We converted velocity anomalies from the global shear wave tomography model SEMUCBWM1 (22) to temperature using HeFESTo (23),

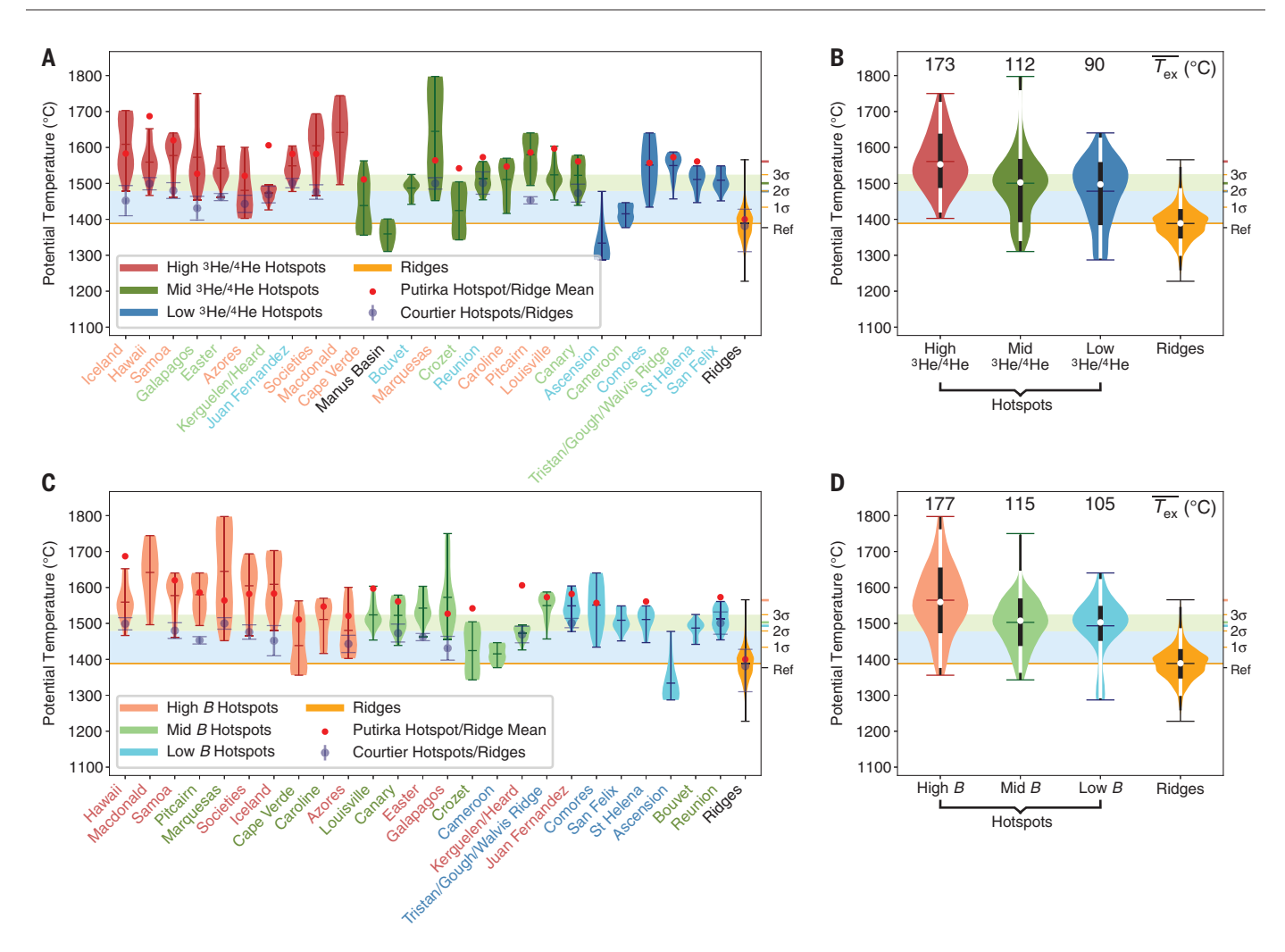


Fig. 3. Potential temperature of hotspots with different  ${}^3\text{He}/{}^4\text{He}$  ratios or geometrical buoyancy flux (B). Violin plots of the inferred  $T_p$ , for plume hotspots sorted by  ${}^3\text{He}/{}^4\text{He}$  and B. Red, green, and blue ticks on the right are the  $\overline{T_{ex}}$  for the corresponding group. Ticks and shaded regions as in Fig. 2.  $\overline{T_p}$  of ridges in the yellow violins. (A) From left to right: dark red, high (>15.7 Ra); dark green, mid; and dark blue, low ( $\leq$ 9 Ra)  ${}^3\text{He}/{}^4\text{He}$ . Purple and red circles as in Fig. 2. Hotspot names colored after groups from B. (B) Hotspots stacked by high, mid, and low (red, green, and blue)  ${}^3\text{He}/{}^4\text{He}$  and compared with

ridges (yellow). Black and white bars as in Fig. 2B. ( $\mathbf{C}$ ) From left to right: light red, high (>0.66 Mg/s); light green, mid; and light blue, low ( $\leq$ 0.19 Mg/s) B. Purple and red circles as in (A). Hotspot names colored after groups from  $^3\text{He}/^4\text{He}$ . ( $\mathbf{D}$ ) As in (B), but stacking B. For both  $^3\text{He}/^4\text{He}$  and B, when comparing temperature of the "high" group and the "mid" plus "low" group hotspots (plume hotspots or all hotspots), Welch's t test gives a P value of  $\leq$ 0.04. Note that 9 Ra corresponds to  $1\sigma$  above MORB average (see text for more details).

a self-consistent thermodynamic model of the phase assemblage of the mantle and its physical properties (21). SEMUCB-WM1 (22) uses full waveform inversions and accurate forward wavefield computations and—as is crucial for inferring temperature—has some of the most robust estimates of absolute velocities in the upper mantle (24). SEMUCB-WM1 also shows 26 oceanic hotspots with well-resolved plumes (6) in our catalog. The reference adiabat, extracted velocities for ridges and hotspots, velocity-to-temperature conversions, and inferred temperatures are shown in fig. S1, and our compiled dataset with the temperature inferred from all seismic models (22, 25-28) can be found in data S1.

Whereas Dalton *et al.* (19) found temperature to be the primary driver of MORB major-

element compositional variability and seismic velocity variations, we went a step further and started with the null hypothesis that seismic anomalies in both the subridge and the subhotspot mantle are due to temperature alone. Further, we assumed that the major element source of mantle melting beneath hotspots and ridges is identical.

Our reference mantle composition was depleted MORB mantle (DMM) (29) with a reference adiabat of 1377°C (1650 K) (21), consistent with previous studies (4, 19) and MORB formation (30). At each hotspot, and every depth interval, we searched for the local minimum  $V_{\rm S}$  anomaly ( $\delta \ln V_{\rm S}$ ), which translates to the highest mantle  $T_{\rm P}$ , within a search radius R centered around the hotspot. We set R to 500 km at Earth's surface to account for the

possible lateral deflection of the plume conduit by the "mantle wind" (Fig. 1B) (21). For ridges, we took the average seismic velocity as representative of the ambient mantle that melts to form MORB. We expect the average temperature to be more representative of their dynamical origin, as ridges are largely the result of passive return flow away from slabs and have no undisputed slow anomalies throughout the entire upper mantle (21). Hence, at each ridge segment, for every depth interval, we averaged all  $\delta \ln V_{\rm S}$  values in a disk of radius R, centered on the ridge segment. By using the local highest temperature for hotspots and the local average temperature beneath each ridge segment, we maximized the inferred  $T_{\rm ev}$ between ridges and hotspots (21). Even in this conservative case, optimal for making hotspots hotter than ridges, we found that >10% of oceanic hotspots [~15% of plume-fed hotspots (6)] are not resolvably hotter than ridges  $(T_{\rm ex} < 50$  °C). Had we chosen the local highest temperature for ridges, as we did for hotspots, then ~70% of oceanic hotspots (~80% of plume-fed hotspots) would not be hotter than ridges.

The effects of limited resolution, smoothing, and damping in seismic tomography models broaden and reduce the amplitude of  $\delta \ln V_{\rm S}$ , leading to lower inferred temperatures. This may be especially true for the local minimum  $\delta ln V_S$  extracted beneath hotspots compared with the broad average  $\delta \ln V_{\rm S}$  beneath midocean ridges. We attempted to correct for these effects beneath hotspots by scaling up  $\delta \ln V_{\rm S}$  by a constant scaling factor f(21). For SEMUCB-WM1 (22), three-dimensional (3D) synthetic resolution tests (6, 22) suggest a conservative scaling factor of f = 2 for plumes that have a core radius [cut off at half peak  $\delta \ln V_{\rm S}(2I)$  of 150 km in the upper mantle. To assess both the resolving power of SEMUCB-WM1 for narrower conduits and the appropriate corresponding f value, we performed two additional 3D synthetic resolution tests (fig. S2) for 100 km radius conduits under Ascension ( $T_{\rm ex}$  = -10°C) and Cameroon ( $T_{\rm ex}$  = 27°C), two cold hotspots. This complements existing resolution tests on Hawaii and Iceland (6). For narrower plumes, f may, depending on resolution, be greater (figs. S2 and S3) (21), but not by enough to alter our main conclusions.

In Fig. 2, we show violin plots (21) of the stacked inferred temperature for all oceanic hotspots and ridge segments at all depths (260 to 600 km). The width of each violin column represents the number density of  $T_p$ . The  $\overline{T_{\rm p}}$  for all ridges is 1388° ± 45°C (1 $\sigma$ ), very close to the 1377°C reference adiabat. The  $\overline{T_p}$  of all oceanic hotspots is  $1527^{\circ} \pm 95^{\circ}$ C, resulting in an average  $T_{\rm ex}$  ( $\overline{T_{\rm ex}}$ ) of 139°C, which spreads over a large range of  $T_{\rm ex}$  for individual hotspots. Cluster analysis (Fig. 2) (21) suggests three distinct groups of hotspots: hot  $(\overline{T_{\rm ex}})$  = 199°C), warm ( $\overline{T_{\rm ex}}$  = 104°C), and cold ( $\overline{T}_{\rm ex}$  = -10°C). For 26 oceanic hotspots associated with seismically resolved plumes [i.e., plumefed hotspots as defined in (6), where we expect the inferred  $T_p$  to be most reliable, as the seismic anomaly is visible through much of the mantle], the  $\overline{T}_p$  (1519° ± 93° versus 1527° ± 95°C) and  $\overline{T_{\rm ex}}$  (131° versus 139°C) are essentially unchanged compared with all oceanic hotspots. We thus focused only on plume-fed hotspots (Fig. 2A, black outlines).

The  $T_{\rm ex}$  of the four hotspots (~15% of the 26 hot spots considered) that are cold (–54°  $\leq$  $T_{\rm ex} \leq 36^{\rm o}{\rm C})$  all fall within  $1\sigma$  (45°C) of the ridge  $\overline{T_{\rm p}}$ . For the 10 hotspots (~40%) that are warm  $(50^{\circ} \le T_{\rm ex} \le 136^{\circ}{\rm C})$ , the  $T_{\rm ex}$  falls within the ridge 3σ (135°C). Only 6 of the 10 warm hot-

spots have sufficiently high  $T_{\rm ex}$  to match or exceed the minimum dynamical limit for mantle plumes with a 100 km radius to rise at 10 cm/year (138°C) (table S1) (21). Thus, even warm hotspots are barely hot and buoyant enough to actively upwell. The remaining 12 hot hotspots have  $T_{\rm ex} \ge 155$  °C, beyond the ridge  $3\sigma$  and well above the dynamical limit. Taken at face value, our results suggest that nearly a third (N=8) of plume-fed hotspots are either not resolvably hotter than ridges or not beyond the minimum dynamical limit ( $T_{\rm ex} \leq 100$  °C). The presence of three classes of hotspots, including cold hotspots, is robust and independent of our choice of seismic model (fig. S4) or reference profile (fig. S5). It is of interest that the cutoff between hot and warm hotspots from the cluster analysis (136°C) matches the  $T_{\rm ex}$  needed for a 100 km radius plume to rise at 10 cm/year (138°C) (21) (table S1). We use this plume radius and terminal speed in the main text for all calculations, unless otherwise noted.

We found that the  $\overline{T_{\rm p}}$  for ridges (1388° ± 45°C) is consistent with Courtier et al.'s (4) and Putirka's (14) petrological estimates (1381°C and  $1400^{\circ} \pm 35^{\circ}$ C, respectively) and Dalton et al.'s (19) hybrid thermometer (1385°  $\pm$  40°C). Our estimate of the  $\overline{T_{\rm ex}}$  for plume-fed hotspots  $(131^{\circ} \pm 77^{\circ}C)$  lies between those of Courtier et al. (4) and Putirka (14) (91°  $\pm$  24°C and 177°  $\pm$ 57°C, respectively) (Fig. 2 and figs. S6 and S7) (21). We note that Courtier et al. (4) also found hotspots with  $T_{\rm ex}$  as low as 50°C, below the typical lower bound of 100°C of other petrological studies (14, 31) but in agreement with our inferences.

We need to evaluate whether our null compositional hypothesis is valid by allowing for the presence of a substantial fraction of recycled crust in the plume source (32). We expect the addition of recycled crust (eclogite) to increase the inferred  $T_{\rm ex}$  because eclogite is seismically faster than DMM (33). Mechanically mixing 10 and 25% normal N-MORB (normal MORB) (29) with DMM in the hotspot mantle source (21) increases the inferred plumefed hotspot  $\overline{T}_{\rm p}$  by 14°C (1533° ± 97°C) and 35°C (1554°  $\pm$  107°C), respectively, compared with the eclogite-free results ( $\overline{T_{\rm p}}\,$  of 1519°  $\pm$  93°C). Even after adding 25% eclogite, 8% of plume-fed hotspots are still cold ( $T_{\rm ex} \le 45$  °C) (fig. S8).

However, the addition of a recycled crustal component comes at a substantial dynamical cost. Any additional eclogitic fraction increases density substantially and requires higher  $T_{\rm ex}$ to overcome the negative buoyancy. For example, plumes with 25% recycled crust would need a  $T_{\rm ex}$  of 368°C (142°C for 10%) just to be neutrally buoyant in the upper mantle (table S1) (21), but they gain only an additional 35°C from the presence of eclogite in the seismic velocity-to-temperature conversion. A  $T_{\rm ex}$  of 368°C is consistent with prior estimates (34) for the upper temperature bound for eclogitebearing plumes to remain neutrally buoyant at the bottom of the lithosphere. At such a  $T_{\rm ex}$ threshold, all hotspots with 25% added eclogite have insufficient  $T_{\rm ex}$  to remain neutrally buoyant, let alone rise actively. At 10% eclogitic fraction, >40% of all plume-fed hotspots remain below the neutral buoyancy threshold (142°C). Therefore, the addition of eclogite cannot explain cold hotspots.

The existence of cold hotspots appears robust both from our results and recent work. A petrological study at Cameroon (35) and a seismological study at Ascension (36) show lower  $T_{\rm ex}$  (~50°C or less;  $T_{\rm p}$  of 1400° to 1430°C), in agreement with our inferences for these hotspots. Low petrological  $T_{\rm ex}$  values have been found for Juan Fernández (37) and Pitcairn (Gambier Island) (38), although these appear as hot hotspots in our estimates. This opens the possibility that, in some cases, we may have overestimated  $T_{\rm ex}$  for some plumes, which would strengthen our conclusions.

Low  $T_{\rm ex}$  values would seem to make it hard for plumes to rise rapidly enough without losing buoyancy. A minimum  $T_{\rm ex}$  of ~135°C is needed for pure DMM plumes with a 100 km radius to rise at ~10 cm/year (16) in the upper mantle (21), consistent with the dynamical limit (17) and simulations (39). Plumes of the same radius containing eclogite require much higher  $T_{\rm ex}$  to rise at the same velocity (>300°C for 10% fraction) (table S1). Envisioning cold, or even warm, hotspots as the same dynamical entities as hot hotspots is difficult.

One hypothesis proposed by Courtillot et al. (40) suggests that cold and warm hotspots are fed by passive upwellings or have a shallow source (3). A shallow source for pure DMM hotspots may be possible if they are generated by edge-driven or small-scale convection (41) or by sublithospheric drainage (42). Alternatively, cold and warm hotspots may still be fed by deep plumes that become trapped and cooled by small-scale convection in the upper mantle (43). In either case, these plumes will have small or even negligible  $T_{\rm ex}$  in the deeper upper mantle. This could be the case for some cold hotspots without clear age progressions, such as Cameroon (42) ( $T_{\rm ex} = 27^{\rm o}$ C) near the West African passive margin. Or these plumes may be weak ( $T_{\rm ex} \sim 50^{\rm o}$ C), as suggested by geophysical (36) and geochemical (44) studies beneath Ascension. For narrower plumes (<50 km core radius), it may be that global tomography is unable to resolve them in the upper mantle. This may be the case for Cape Verde (45), which has a relatively high <sup>3</sup>He/<sup>4</sup>He signal [15.7 Ra (46)] but low inferred  $T_{\rm ex}$  in our model and is well resolved in the lower mantle (6). But it is not the case for Ascension and Cameroon, two cold plumes that are resolved even at core radii of 50 km (fig. S2) (21). A core radius of <35 km would be required for the hottest cold

plume ( $T_{\rm ex}$  = 36°C) to equal the  $\overline{T_{\rm ex}}$  for hot hotspots (199°C), as our synthetic resolution tests suggest (21). Narrower plumes, however, would need to rise faster, and thus be hotter than the minimum dynamical limit, so as not to lose their buoyancy and be buffeted by the mantle wind.

For hotspots with a small fraction of recycled oceanic crust (e.g.,  $\sim$ 5%), a  $T_{\rm ex}$  of  $\sim$ 50°C is enough to overcome the excess density of eclogite. Such low  $T_{\rm ex}$  is enough to allow a thermochemical plume to rise with the help of broad passive upward return flow that occurs above large low shear wave velocity provinces (LLSVPs), a return flow that complements downward flow at global subduction zones (21). Broad passive flow can contribute half [~1.5 to 3 cm/year (47)] of the velocity needed by low  $T_{\rm ex}$  plumes to rise fast enough to keep their buoyancy (21), the other half arising from their  $T_{\rm ex}$ . We cannot rule out the possibility that the cold hotspots are wet, which lowers the melting temperature at shallow depths and leads to decompression melting (48). Whatever the explanation, these hotspots do not fit the classical plume model.

On the other hand, hotspots with the highest  $T_{\rm ex}$  do fit the classical model, as they are more than hot enough to rise actively. These hot plumes are also associated with many of the largest buoyancy fluxes and the highest <sup>3</sup>He/<sup>4</sup>He. Figure 3 shows a series of violin plots of the stacked  $T_p$  of plume-fed hotspots, colored and sorted by <sup>3</sup>He/<sup>4</sup>He (12) (Fig. 3, A and B) or geometrical buoyancy flux B(5, 2I)(Fig. 3, C and D). We use  ${}^{3}\text{He}/{}^{4}\text{He} \leq 9$  Ra and  $B \le 0.19$  Mg/s as the threshold criterion for hotspots with low flux and He ratios, where 9 Ra is the 1 $\sigma$  deviation from the MORB mean (8 Ra) (7), and both correspond to the lowest 30th percentile. We further divide the remaining hotspots into high ( ${}^{3}\text{He}/{}^{4}\text{He} > 15.7 \text{ Ra}$ ; B >0.66 Mg/s), the top 70th percentile, and intermediate  $(9 < {}^{3}\text{He}/{}^{4}\text{He} \le 15.7 \text{ Ra}; 0.19 < B \le 0.66 \text{ Mg/s})$ categories. We find that the  $\overline{T_{\rm ex}}$  of hotspots reduces as a function of decreasing <sup>3</sup>He/<sup>4</sup>He or B (Fig. 3 and figs. S9 and S10). These results directly confirm the relationships between higher plume temperature and extreme <sup>3</sup>He/<sup>4</sup>He and buoyancy flux proposed by Jackson et al. (12) using seismic velocity at 200 km depth, and by Putirka (14) using petrologically derived temperatures.

For Iceland and Hawaii, the two hotspots with the highest  ${}^{3}\text{He}/{}^{4}\text{He}$ , we find a  $T_{p}$  of  $1609^{\circ}\text{C} (T_{\text{ex}} = 221^{\circ}\text{C}) \text{ and } 1559^{\circ}\text{C} (T_{\text{ex}} = 171^{\circ}\text{C}),$ respectively, firmly in the hot hotspot cluster (Fig. 2). Iceland's higher  $T_{\rm ex}$  compared with Hawaii is more compatible with its higher <sup>3</sup>He/<sup>4</sup>He signal [up to 47.5 Ra (49) versus 35.3 Ra (50)] and estimates of its buoyancy flux (21, 51) but is not compatible with the greater lithospheric thickness beneath Hawaii (48).

If high <sup>3</sup>He/<sup>4</sup>He domains are associated with primordial and denser material, it may

be that only the more buoyant (hotter) plumes can entrain it and rise to the surface (12). High <sup>3</sup>He/<sup>4</sup>He in OIBs is geographically correlated to the two LLSVPs (Fig. 1A) in the lowermost mantle (10). LLSVPs may be denser and chemically distinct (52), compatible with a reservoir of dense oceanic crust or primordial material with high <sup>3</sup>He/<sup>4</sup>He (53). Our results suggest that hot hotspots are indeed thermochemical in nature but are hot and buoyant enough to entrain LLSVP material with high <sup>3</sup>He/<sup>4</sup>He.

We find a  $\overline{T_{\rm ex}}$  of 205°C for five hotspots overlying large ultra low velocity zones ("mega-ULVZs") at the CMB: Iceland, Hawaii, Samoa, and Marquesas (54) as well as Galápagos (55) (fig. S11A). These hotspots also have the highest <sup>3</sup>He/<sup>4</sup>He, with the exception of Marquesas (54), which has a moderately-high <sup>3</sup>He/<sup>4</sup>He but high B. If these mega-ULVZs are broad regions of partial melt they may provide roots for some hot, strong plumes (54). They may also represent a core-mantle interaction zone, which may be the source of ancient isotopic anomalies (56) in hotspot lavas. Two other classes of plumes appear to be cooler and less thermally buoyant and give rise to low-flux hotspots. They do not appear to entrain deepseated primordial domains—possibly because they are too cold and thus insufficiently buoyant to entrain a deep and dense high  ${}^{3}\text{He}/{}^{4}\text{He}$ domain (12)—but they may provide important clues to shallower mantle processes such as slow-rising plumes and small-scale convection.

### REFERENCES AND NOTES

- W. J. Morgan, Nature 230, 42-43 (1971).
- 2. N. H. Sleep, Spec. Pap. Geol. Soc. Am. 430, 29-45 (2007).
- D. L. Anderson, Aust. J. Earth Sci. 60, 657-673 (2013).
- 4. A. M. Courtier et al., Earth Planet. Sci. Lett. 264, 308-316 (2007) S. D. King, C. Adam, Phys. Earth Planet. Inter. 235, 66-83 (2014).
- S. W. French, B. Romanowicz, Nature 525, 95-99 (2015).
- D. W. Graham, Rev. Mineral, Geochem. 47, 247–317 (2002)
- M. G. Jackson et al., Proc. Natl. Acad. Sci. U.S.A. 117, 30993-31001 (2020)
- F. M. Stuart, S. Lass-Evans, J. G. Fitton, R. M. Ellam, Nature 424, 57-59 (2003).
- 10. C. D. Williams, S. Mukhopadhyay, M. L. Rudolph, B. Romanowicz, Geochem. Geophys. Geosyst. 20, 4130-4145 (2019).
- 11. A. M. Jellinek, M. Manga, Rev. Geophys. 42, RG3002 (2004).
- 12. M. G. Jackson, J. G. Konter, T. W. Becker, Nature 542, 340-343 (2017).
- 13. H. Samuel, C. G. Farnetani, Earth Planet. Sci. Lett. 207, 39-56 (2003).
- 14. K. Putirka, Geology 36, 283 (2008).
- 15. C. Herzberg, P. D. Asimow, Geochem. Geophys. Geosyst. 9, Q09001 (2008).
- 16. B. Steinberger, M. Antretter, Geochem. Geophys. Geosyst. 7, 011018 (2006).
- 17. M. Albers, U. R. Christensen, Geophys. Res. Lett. 23, 3567-3570 (1996)
- 18. D. Mckenzie, M. J. Bickle, J. Petrol. 29, 625-679 (1988). 19. C. A. Dalton, C. H. Langmuir, A. Gale, Science 344, 80-83 (2014)
- 20. A. Gale, C. A. Dalton, C. H. Langmuir, Y. Su, J. G. Schilling, Geochem. Geophys. Geosyst. 14, 489-518 (2013).
- 21. Materials and methods are available as supplementary materials.
- 22. S. W. French, B. A. Romanowicz, Geophys. J. Int. 199. 1303-1327 (2014).
- L. Stixrude, C. Lithgow-Bertelloni, Geophys. J. Int. 184, 1180-1213 (2011).
- 24. M. Meschede, B. Romanowicz, Geophys. J. Int. 200, 1078-1095 (2015).
- 25. N. A. Simmons, A. M. Forte, L. Boschi, S. P. Grand, J. Geophys. Res. 115, B12310 (2010).

- 26. J. Ritsema, A. Deuss, H. J. Van Heijst, J. H. Woodhouse, Geophys. J. Int. 184, 1223-1236 (2011).
- 27. A. J. Schaeffer, S. Lebedev, Geophys. J. Int. 194, 417-449 (2013)
- 28. E. Debayle, F. Dubuffet, S. Durand, Geophys. Res. Lett. 43, 674-682 (2016).
- 29. R. K. Workman, S. R. Hart, Earth Planet. Sci. Lett. 231, 53-72 (2005).
- 30 R S White T A Minshull M I Rickle C I Robinson J. Petrol. 42, 1171-1196 (2001).
- 31. C. Herzberg et al., Geochem. Geophys. Geosyst. 8, Q02006 (2007).
- 32. S. Pugh, J. Jenkins, A. Boyce, S. Cottaar, Earth Planet. Sci. Lett. **561**. 116813 (2021).
- 33. W. Xu, C. Lithgow-Bertelloni, L. Stixrude, J. Ritsema, Earth Planet. Sci. Lett. 275, 70-79 (2008).
- 34. M. Pertermann, M. M. Hirschmann, J. Petrol. 44, 2173-2201 (2003).
- 35. C. N. Ngwa, T. H. Hansteen, C. W. Devey, F. M. van der Zwan. C. E. Suh, Lithos 288-289, 326-337 (2017).
- 36. T. A. Minshull, N. J. Bruguier, J. M. Brozena, Geology 26, 115-118 (1998).
- 37. J. Reves et al., Geochim, Cosmochim, Acta 257, 311-335 (2019) 38. H. Delavault, C. Chauvel, A. Sobolev, V. Batanova, Earth Planet.
- Sci. Lett. 426, 23-35 (2015). 39. M. Arnould, N. Coltice, N. Flament, C. Mallard, Earth Planet Sci. Lett. 547, 116439 (2020).
- 40. V. Courtillot, A. Davaille, J. Besse, J. Stock, Earth Planet, Sci. Lett. 205, 295-308 (2003).
- 41. S. D. King, J. Ritsema, Science 290, 1137-1140 (2000).
- 42. A. R. Guimarães, J. G. Fitton, L. A. Kirstein, D. N. Barfod, Earth Planet. Sci. Lett. 536, 116147 (2020).
- 43. S. French, V. Lekic, B. Romanowicz, Science 342, 227-230 (2013).
- 44. E. Bourdon, C. Hémond, Mineral, Petrol. 71, 127-138 (2001).
- 45. X. Liu, D. Zhao, Geophys. J. Int. 225, 872-886 (2021).
- 46. R. Doucelance, S. Escrig, M. Moreira, C. Gariépy, M. D. Kurz, Geochim. Cosmochim. Acta 67, 3717-3733 (2003).
- 47. A. M. Forte et al., Earth Planet. Sci. Lett. 295, 329-341 (2010).
- 48. J. G. Fitton, R. Williams, T. L. Barry, A. D. Saunders, J. Petrol. 61. egaa111 (2020).
- 49. S. Harðardóttir, S. A. Halldórsson, D. R. Hilton, Chem. Geol. 480, 12-27 (2018).
- 50. P. J. Valbracht, T. Staudacher, A. Malahoff, C. J. Allègre, Earth Planet. Sci. Lett. 150, 399-411 (1997)
- 51. R. Parnell-Turner et al., Nat. Geosci. 7, 914-919 (2014).
- 52. M. Ishii, J. Tromp, Science 285, 1231-1236 (1999).
- 53. T. D. Jones, R. Maguire, P. van Keken, J. Ritsema, P. Koelemeijer, EarthArXiv [Preprint] (2021). https://doi.org/ 10.31223/osf.jo/k98p7.
- 54. D. Kim, V. Lekić, B. Ménard, D. Baron, M. Taghizadeh-Popp, Science 368, 1223-1228 (2020).
- 55. S. Cottaar, Z. Li, AGU Fall Meeting Abstracts 2019, DI33A-04
- 56. A. Mundl-Petermeier et al., Geochim. Cosmochim. Acta 271, 194-211 (2020).

### **ACKNOWLEDGMENTS**

We thank C. A. Dalton for providing data for comparison and K. D. Putirka, C. D. Williams, L. Stixrude, and J. Aurnou for constructive discussions. Funding: This work was made possible by NSF grant FAR-1900633 to C.R.L.-B. FAR-1900652 to M.G.L. and EAR-1758198 to B.R. C.R.L.-B. was further supported by the Louis B. and Martha B. Slichter Endowment for Geosciences. Author contributions: X.B. analyzed the hotspot catalog provided by M.G.J. and conducted the thermodynamic conversions with the help of C.R.L.-B. M.G.J. aided the geochemical analysis and interpretation B.R. performed synthetic plume tests in SEMUCB-WM1 and aided with the interpretation of tomographic results. X.B. led the writing of the manuscript, and all authors discussed the results and edited the manuscript. Competing interests: The authors declare that they have no competing interests. Data and materials availability: The thermodynamic simulation package HeFESTo (23) is available at https://github.com/stixrude/HeFESToRepository. The parameter set is at https://github.com/stixrude/HeFESTo\_Parameters\_310516.

## SUPPLEMENTARY MATERIALS

science.org/doi/10.1126/science.abj8944 Materials and Methods Figs. S1 to S11 Table S1 References (57-89) Data S1 8 June 2021: accepted 9 November 2021

10.1126/science.abj8944